

Partitioned solver for strongly coupled fluid–structure interaction

Charbel Habchi^{a,b}, Serge Russeil^{a,c,*}, Daniel Bougeard^{a,c}, Jean-Luc Harion^{a,c}, Thierry Lemenand^d, Akram Ghanem^d, Dominique Della Valle^{d,e}, Hassan Peerhossaini^{d,f}

^a EMDouai, El, F-59500 Douai, France

^b Energy and Thermo-Fluid Group ETF, School of Engineering, Lebanese International University LIU, PO Box 146404, Mazraa, Beirut, Lebanon

^c Université Lille Nord de France, F-59000 Lille, France

^d ThermoFluids, Complex Flows and Energy Research Group, Laboratoire de Thermocinétique de Nantes – CNRS UMR 6607, Nantes University, F-44306 Nantes, France

^e ONIRIS, F-44322 Nantes, France

^f Univ Paris Diderot, Sorbonne Paris Cité, Institut des Energies de Demain (IED), F-75013 Paris, France

ARTICLE INFO

Article history:

Received 5 December 2011

Received in revised form 18 September 2012

Accepted 6 November 2012

Available online 15 November 2012

Keywords:

Arbitrary Lagrangian–Eulerian

Aitken's under-relaxation

Elastic large deformation

St. Venant–Kirchhoff material

Finite volume method

OpenFOAM

ABSTRACT

In this work a fluid–structure interaction solver is developed in a partitioned approach using block Gauss–Seidel implicit scheme. Finite volume method is used to discretize the fluid flow problem on a moving mesh in an arbitrary Lagrangian–Eulerian formulation and by using an adaptive time step. The pressure–velocity coupling is performed by using the PIMPLE algorithm, a combination of both SIMPLE and PISO algorithms, which permits the use of larger time steps in a moving mesh. The structural elastic deformation is analyzed in a Lagrangian formulation using the St. Venant–Kirchhoff constitutive law, for non-linear large deformations. The solid structure is discretized by the finite volume method in an iterative segregated approach. The automatic mesh motion solver is based on Laplace smoothing equation with variable mesh diffusion. The strong coupling between the different solvers and the equilibrium on the fluid–structure interface are achieved by using an iterative implicit fixed-point algorithm with dynamic Aitken's relaxation method. The solver, which is called vorflexFoam, is developed using the open source C++ library OpenFOAM. The solver is validated on two different benchmarks largely used in the open literature. In the first one the structural deformation is induced by incompressibility. The second benchmark consists on a vortex excited elastic flap in a Von Karman vortex street. Finally, a more complex case is studied including two elastic flaps immersed in a pulsatile flow. The present solver detects accurately the interaction between the complex flow structures generated by the flaps and the effect of the flaps oscillations between each other.

© 2012 Elsevier Ltd. All rights reserved.

1. Introduction

Fluid–structure interaction is a complex multi-physics issue with contiguous domains consisting generally on viscous fluid flow over elastic solid structures. The elastic structure deforms due to fluid action; mainly pressure and viscous stress. The development of robust numerical solvers for fluid–structure interaction problems is a fundamental issue in many engineering fields, such as heat exchangers and chemical reactors, marine cables and petroleum production risers, aeronautics, vortex induced vibration and noise, hemodynamics and blood vessel dynamics [1–7].

Two numerical methods can be distinguished as either monolithic or partitioned. In the monolithic approach, the complete non-linear system of fluid flow and solid displacement equations

are solved simultaneously and are discretized in time and space in the same manner [7–11]. This fully-coupled or direct approach is known to be highly robust and stable for very strong fluid–structure interaction including for example phase transformation in material processing, viscoplastic deformation, fracturing due to shocks or detonation [12,13]. However, monolithic methods represent less modularity and require more coding than partitioned approach in which flow and structural equations are solved by using independent suitable algorithms and discretization methods [14–18]. In fact, in the implicit partitioned Dirichlet–Neumann approach, the flow and structural equations are solved separately and the coupling is limited only to the fluid–structure interface. Therefore, an iterative algorithm must be used to handle the communication between both flow and structural solvers and to enforce the equilibrium on the fluid–structure interface. This means that the fluid flow and the structural deformation are solved successively within an iterating loop until that the difference between the flow and structural solutions, such as the interface displacement, is smaller than a given convergence criterion. The most commonly

* Corresponding author at: Ecole des Mines de Douai, Département Energétique Industrielle, 941 Rue Charles Bourseul, CS 10838, 59508 Douai Cedex, France. Tel.: +33 3 27 71 23 88; fax: +33 3 27 71 29 15.

E-mail address: serge.russeil@mines-douai.fr (S. Russeil).

used coupling methods are the fixed-point method (also called block Gauss–Seidel method) [19–21], the interface Newton–Krylov and the quasi-Newton methods [21–25].

Many studies [14–15,18,20,23, 24,26–28] have shown that, the use of a fixed-point method with dynamic under-relaxation is highly efficient and easy to implement in partitioned approaches. When the coupling between the fluid flow and the structural deformation is strong, due to low solid stiffness or high fluid/structure density ratio, the iterations converge slowly and they even may diverge if the relaxation parameter value is not well chosen. Therefore, the fixed-point iterations can be stabilized and accelerated by using the Aitken relaxation method where the relaxation parameter is adapted at each iteration using the solution of two previous iterations [14,20,29].

Solving fluid–structure interaction problems by implicit fixed-point method can be partitioned into three coupled solvers.

The first one is the fluid flow which solves, for instance, the incompressible Navier–Stokes equations for viscous fluid. In fluid–structure interaction problems, the computational domain of the fluid flow is deforming with the fluid–structure interface displacement, and thus the Arbitrary Lagrangian–Eulerian (ALE) formulation is used to solve the Navier–Stokes equations on a deforming mesh [30–33].

The second solver deals with the structural deformation equations. Generally, the elastic structural deformation can be solved by using the simple linear formulation by considering the constitutive model for a Hookean solid [8,34]. However, for large structural displacement with high strain rates it is more suitable to use the nonlinear formulation where the St. Venant–Kirchhoff constitutive model is used for structural analysis [18,35,36]. In contrast to well established finite element methods for computational solid mechanics [6,37,38], Jasak and Weller [34] discretized the linear elastic deformation problem, in Lagrangian formulation, by using an optimized finite volume method. In this approach, the convective terms are discretized implicitly and the diffusive terms are discretized explicitly, accelerating thus the convergence of the final solution. In the present paper, the nonlinear elastic deformation problem is discretized by using the same method proposed by Jasak and Weller [34] and which was recently used by Olivier et al. [36].

The third solver concerns the internal mesh motion which may be computed using different numerical approaches depending on either the motion is pure translation, rotation or both translation and rotation as in the present study and in [33,39–44]. In the present study, the internal mesh motion is solved by using the Laplace smoothing equation [39,41]. This solver takes the mesh motion at the fluid–structure interface as boundary conditions and solves the unknown mesh motion equation in the internal fields. Variable mesh diffusivity is used to maintain good mesh quality especially near the moving boundary.

In the present study, the open source C++ library OpenFOAM [42,43] is used to implement the different numerical solvers and algorithms as explained in Sections 2 and 2.4. The originality of the solver developed here is that it uses a partitioned finite volume method to solve fluid–structure interaction with implicit fixed point scheme and dynamic relaxation insuring strong coupling between the solvers. The solid displacement is modeled by the nonlinear elastic deformation and Navier–Stokes equations are solved in ALE approach. As it uses an open source C++ library, this solver is available¹ for scientific community working on fluid–structure interaction problems and it can be simply modified to meet the special need of users. Section 4 is devoted to the validation of the

numerical solver by comparing the present results with those obtained from the literature. In this same section, a more complex case is studied consisting of two elastic structures fixed on the bottom wall in a pulsatile channel flow. Concluding remarks are given in Section 5.

2. Governing equations

2.1. Flow equations

The flow field is governed by the unsteady Navier–Stokes equations for an incompressible viscous flow. The continuity and momentum equations are respectively given by:

$$\nabla \cdot \mathbf{u}_f = 0 \quad (1)$$

$$\frac{\partial \mathbf{u}_f}{\partial t} + \mathbf{u}_f \cdot \nabla \mathbf{u}_f = -\frac{\nabla p}{\rho_f} + \nu_f \nabla^2 \mathbf{u}_f \quad (2)$$

Eqs. (1) and (2) are satisfied in the fluid reference domain $\Omega_{f,0}$. For flows without moving mesh, these governing equations can be discretized by using the Eulerian description where the mesh is held fixed [32]. In the Lagrangian formulation, the mesh is fixed to the moving boundary and it moves with it. However, these strategies are not valid for computational domains which deform in time as for instance [32]. Therefore, an arbitrary Lagrangian–Eulerian (ALE) formulation [32] is used to handle the flow equations on a deforming mesh, as described in the next section.

2.2. Arbitrary Lagrangian–Eulerian mapping

The arbitrary Lagrangian–Eulerian (ALE) formulation [32] is in fact the most commonly used description for fluid–structure interaction including arbitrary boundary deformation [33,44–46]. The motion of the interface near the moving structure imposes a convective governed flow that is solved by the Lagrangian description. Far away from the structure, the mesh velocity $\mathbf{u}_{m,f}$ tends to zero so the equations tend to the Eulerian description.

The fluid domain displacement $\mathbf{d}_{m,f}$ is an extension of the solid displacement $\mathbf{d}_s^{I_0}$ from the fluid–structure interface Γ_0 to the internal fluid reference domain $\Omega_{f,0}$. Thus, initially, $\Delta \mathbf{d}_{m,f} = 0$ in $\Omega_{f,0}$ and $\mathbf{d}_{m,f} = \mathbf{d}_s^{I_0}$ on Γ_0 . The ALE mapping is then defined as in Crosetto et al. [7]:

$$\chi(t) : \Omega_{f,0} \rightarrow \Omega_{f,t} \quad (3)$$

$$\mathbf{x}_0 \mapsto \chi_t(\mathbf{x}_0) = \mathbf{x}_0 + \mathbf{d}_{m,f}(\mathbf{x}_0)$$

The fluid domain velocity can be defined by:

$$\mathbf{u}_{m,f} = \left. \frac{\partial \mathbf{d}_{m,f}}{\partial t} \right|_{\mathbf{x}_0} = \left. \frac{\partial \chi_t}{\partial t} \right|_{\mathbf{x}_0} \quad (4)$$

The ALE formulation of the Navier–Stokes equations that are satisfied in the updated fluid domain $\Omega_{f,t}$ is thus [7]:

$$\nabla \cdot \mathbf{u}_f = 0 \quad (5)$$

$$\frac{\partial \mathbf{u}_f}{\partial t} + (\mathbf{u}_f - \mathbf{u}_{m,f}) \nabla \mathbf{u}_f = -\frac{\nabla p}{\rho_f} + \nu_f \nabla^2 \mathbf{u}_f \quad (6)$$

where $(\mathbf{u}_f - \mathbf{u}_{m,f})$ is the convective term; the Eulerian and Lagrangian descriptions are obtained respectively by setting $\mathbf{u}_{m,f} = 0$ or $\mathbf{u}_{m,f} = \mathbf{u}_f$, with $\mathbf{u}_{m,f}$ the mesh velocity in the fluid domain.

2.3. Structural equations

The equation of motion for an elastic isothermal solid structure can be described by the momentum conservation law:

¹ <http://www.cfd-online.com/Forums/openfoam/85087-solver-fsi-strongly-coupled-3.html>.

$$\rho_s \frac{\partial \mathbf{u}_s}{\partial t} = \nabla \cdot \boldsymbol{\sigma}_s - \rho_s (\nabla \mathbf{u}_s) \mathbf{u}_s + \rho_s f_b \quad (7)$$

where \mathbf{u}_s is the solid velocity $\mathbf{u}_s = \partial \mathbf{d}_s / \partial t$ with \mathbf{d}_s the displacement of the structure, $\boldsymbol{\sigma}_s$ is the Cauchy stress tensor and f_b is the resulting body force. Eq. (7) is satisfied in the solid structure domain Ω_s .

In the present study, the St. Venant–Kirchhoff constitutive law, using an iterative segregated approach in a Lagrangian formulation, is implemented to model the elastic structure deformation. This is driven by the fact that this approach is more convenient for large elastic structure deformation where linear elastic solid models fail to describe the structure behavior.

From a Lagrangian point of view, i.e. in terms of the initial configuration at $t = 0$, the momentum balance Eq. (7) is expressed by Eq. (8) which is satisfied in the Lagrangian domain $\Omega_{s,t}$:

$$\rho_s \frac{\partial^2 \mathbf{d}_s}{\partial t^2} = \nabla \cdot (\boldsymbol{\Sigma} \cdot \mathbf{F}^T) + \rho_s f_b \quad (8)$$

with \mathbf{F} the deformation gradient tensor given by:

$$\mathbf{F} = \mathbf{I} + \nabla \mathbf{d}_s^T \quad (9)$$

where \mathbf{I} is the identity.

The second Piola–Kirchhoff stress tensor $\boldsymbol{\Sigma}$ is related to the Green Lagrangian strain tensor \mathbf{G} following [35,36]:

$$\boldsymbol{\Sigma} = 2\mu_s \mathbf{G} + \lambda_s tr(\mathbf{G}) \mathbf{I} \quad (10)$$

with \mathbf{G} given by:

$$\mathbf{G} = \frac{1}{2} (\mathbf{F}^T \cdot \mathbf{F} - \mathbf{I}) \quad (11)$$

here tr is the tensor trace, λ_s and μ_s are Lamé constants which are characteristics of the elastic material. They are linked to the Young modulus E and Poisson's coefficient ν_s by:

$$\lambda_s = \frac{\nu_s E}{(1 + \nu_s)(1 - 2\nu_s)} \quad (12)$$

$$\mu_s = \frac{E}{2(1 + \nu_s)} \quad (13)$$

Replacing \mathbf{G} , $\boldsymbol{\Sigma}$ and \mathbf{F} in Eq. (8) by their expressions from Eqs. (9)–(11) gives:

$$\rho_s \frac{\partial^2 \mathbf{d}_s}{\partial t^2} = \nabla \cdot \left\{ \left[\mu_s \nabla \mathbf{d}_s + \mu_s \nabla \mathbf{d}_s^T + \mu_s \nabla \mathbf{d}_s \cdot \nabla \mathbf{d}_s^T + \lambda_s tr(\nabla \mathbf{d}_s) + \frac{1}{2} \lambda_s tr(\nabla \mathbf{d}_s \cdot \nabla \mathbf{d}_s^T) \right] \cdot (\mathbf{I} + \nabla \mathbf{d}_s) \right\} + \rho_s f_b \quad (14)$$

This equation is solved in a segregated manner following the method proposed by Jasak and Weller [34]. Using the Gauss' theorem, the integral form of Eq. (12) over a cell of volume V and surface S reads:

$$\begin{aligned} \int_V \rho_s \frac{\partial^2 \mathbf{d}_s}{\partial t^2} dV &= \int_S dS \cdot (2\mu_s + \lambda_s) \nabla \mathbf{d}_s \\ &+ \int_V \left\{ \left[\mu_s \nabla \mathbf{d}_s + \mu_s \nabla \mathbf{d}_s^T + \mu_s \nabla \mathbf{d}_s \cdot \nabla \mathbf{d}_s^T + \lambda_s tr(\nabla \mathbf{d}_s) + \frac{1}{2} \lambda_s tr(\nabla \mathbf{d}_s \cdot \nabla \mathbf{d}_s^T) \right] \cdot (\mathbf{I} + \nabla \mathbf{d}_s) \right. \\ &\left. - (2\mu_s + \lambda_s) \nabla \mathbf{d}_s + \rho_s f_b \right\} dV \end{aligned} \quad (15)$$

This equation is solved before the last step in Fig. 1.

Following Jasak and Weller [34], the first term on the right-hand side, which is a diffusive term, is discretized implicitly. The second term on the right-hand side is treated as a source term and discretized in explicit manner. Jasak and Weller [34] show that this discretization method has a significant improvement on the convergence and stability.

2.4. Coupling and boundary conditions

To establish the equilibrium on fluid–structure interface Γ , certain conditions must be respected. Primarily the continuity of displacement \mathbf{d} , mesh velocity \mathbf{u}_m and equilibrium traction $\boldsymbol{\tau}$:

$$\mathbf{d}_s^F = \mathbf{d}_f^F \quad (16)$$

$$\mathbf{u}_s^F = \mathbf{u}_f^F \quad (17)$$

$$\boldsymbol{\tau}_s^F + \boldsymbol{\tau}_f^F = 0 \quad (18)$$

where the superscript F denotes the variable at the fluid–structure interface. Equations (16)–(18) must be satisfied at Γ .

The traction $\boldsymbol{\tau}_f$ is the sum of viscous forces and pressure $\boldsymbol{\tau}_f = p\mathbf{n} + \mu_f \nabla \mathbf{u}_f \cdot \mathbf{n}$ [44,45]. In fact, Eqs. (16) and (17) represent the continuity of the primary quantities at the fluid–structure interface: the displacement $\mathbf{d}_s^F = \mathbf{d}_f^F$ and the velocity $\mathbf{u}_s^F = \mathbf{u}_f^F$; Eq. (18) represents the equilibrium of the dual quantities (action–reaction principle) $\boldsymbol{\tau}_s^F + \boldsymbol{\tau}_f^F = 0$ including viscous stress and pressure.

The pressure and viscous forces (Eq. (16)) of the fluid flow at the fluid–structure interface are transferred to the solid as boundary conditions for the structural solver that computes the displacement and stress field in the structure. The displacement velocity is then used as input to solve the mesh motion. The stress field of the structural domain is transferred to the flow field as a boundary condition on the fluid–structure interface;

$$\boldsymbol{\sigma}_f^F = \nu_f dev(\nabla \mathbf{u}_f + \nabla \mathbf{u}_f^T) \quad (19)$$

where dev is the deviatoric of a matrix \mathbf{A} : $dev(\mathbf{A}) = \mathbf{A} - (1/3)\text{tr}(\mathbf{A})\mathbf{I}$.

Both the fluid and solid domains are initially at rest. No slip boundary conditions are imposed on the fluid/structure interfaces or on the other walls. The outlet is set at zero pressure and zero Neumann for velocity, and a user-defined parabolic velocity profile is set at the flow inlet for the case in question. In fact, these boundary conditions depend on the cases studied in Section 4, where more complete details on boundary conditions are given for each case, especially for the inlet.

3. Numerical procedure

3.1. Spatial and temporal discretization

The open-source C++ toolbox OpenFOAM 1.6-ext [42,45] is used to approximate the fluid flow and structure displacement by using a finite volume approach. The values of all variables are stored in every control volume center using a collocated variable arrangement [45]. A linear scheme with central differencing is used for value interpolation from cell centers to face centers. The surface normal gradients are evaluated at the cell faces and their solution algorithm uses an explicit non-orthogonal correction scheme. Laplacian and gradient terms are discretized by second-order Gaussian integration based on linear interpolation. Gaussian schemes with limited linear differencing interpolation are used for the divergence terms in the flow and structural solvers.

In the present study, a non-uniform unstructured conforming quadrilateral mesh is generated using the software Gambit, and is refined at the wall boundaries and fluid–structure interface to take into consideration the high velocity and pressure gradients in these regions.

Fluid–structure interaction problems with moving solid boundaries require a third coupled solver for an automatic internal mesh motion. This solver consequently deforms the internal fluid domain while maintaining the quality and validity of the

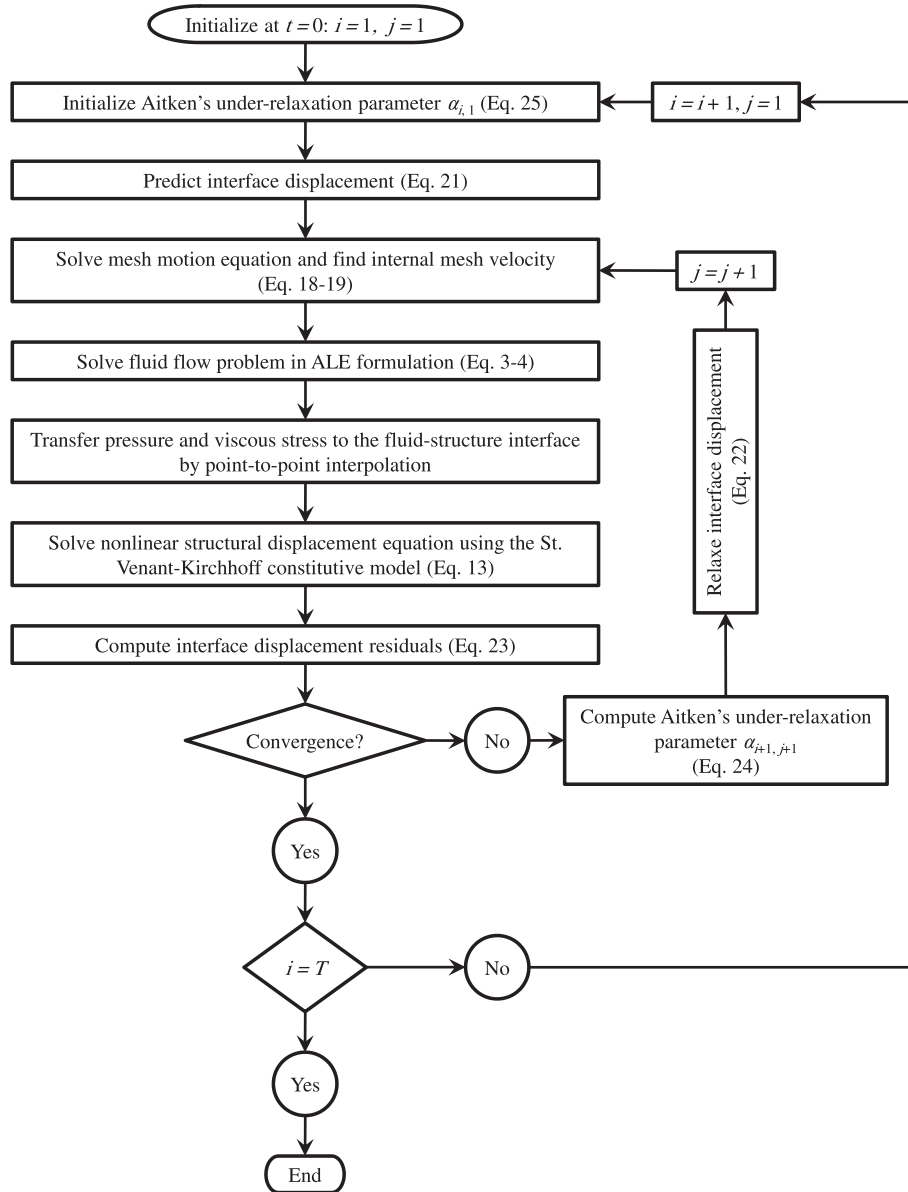


Fig. 1. Simplified flowchart for the method used in the present partitioned solver for strongly coupled nonlinear fluid–structure interaction (i is the time step, from 1 to T , and j is the outer Aitken iterations, from 1 to N).

deforming mesh. In this case, the displacement of the fluid–structure interface, which is the result of the structural solver, is then used as a boundary condition for the mesh motion solver.

Several solvers for the mesh motion can be found in the open literature [33,39,41,44,45] such as Laplace smoothing [47], solid body rotation stress (SBR stress) [48], pseudo-solid equations [49] and radial basis function [33,50,51].

The present study employs the Laplace smoothing equation given by the following expression and discretized by the finite element method:

$$\nabla \cdot (\gamma \nabla \mathbf{u}_m) = 0 \quad (20)$$

where γ is the mesh diffusion coefficient and \mathbf{u}_m the mesh velocity $\mathbf{u}_m = (\mathbf{x}_{t+\delta t} - \mathbf{x}_t)/\delta t$, with \mathbf{x} the mesh position.

When using the Laplace equation, the mesh point movement will be largest near the moving boundary, and this leads to mesh distortion and deterioration [34,47]. Thus the mesh quality can be maintained by using a variable mesh diffusion γ in the Laplacian

operator. Several methods can be used to describe the mesh diffusion coefficient, such as the distance-based method where the diffusion coefficient is a function of cell distance to the nearest moving boundary, and the distortion-energy method based on the cell distortion [45]. It has been shown [39] that an inverse quadratic diffusivity coefficient with the Laplace face decomposition method maintains mesh quality for large boundary translations. Hence, this method is used, and thus the diffusion coefficient is related to the cell distance to the nearest moving boundary ℓ through:

$$\gamma(\ell) = \frac{1}{\ell^2} \quad (21)$$

Eqs. (20) and (21) are included in the third step in Fig. 1.

Temporal discretization is performed using a second order implicit scheme which is unconditionally stable. The time step is automatically adapted during the simulations by using a predefined maximal Courant number $Co_{\max} = 0.4$:

$$Co = \frac{\delta t U_{cf}}{\delta x} \quad (22)$$

Co is the Courant number in a given cell, U_{cf} is the magnitude of the flow velocity at this cell, δx the cell size in the velocity direction and δt the time step. Therefore, by fixing $Co_{\max} = 0.4$, the time step Δt is computed from the minimum value of $\delta t = 0.4(\delta x/U_{cf})$ taken over all fluid cells.

The pressure equation is solved by using a pre-conditioned conjugate gradient (PCG) iterative solver with a diagonal incomplete Cholesky (IC) pre-conditioner used for symmetric matrices. This pre-conditioner is a sparse approximation of the Cholesky factorization which is a decomposition of a Hermitian, positive-definite matrix into the product of a lower triangular matrix and its conjugate transpose. The convergence criterion for the pressure is fixed to 10^{-7} . The velocity–pressure coupling equation uses the asymmetric pre-conditioned bi-conjugate gradient solver (PBICG) with a diagonal incomplete LU decomposition (ILU) pre-conditioner for asymmetric matrices. This pre-conditioner consists in a matrix decomposition of the systems of linear equations, and which writes a matrix as the product of a lower triangular matrix and an upper triangular matrix. The convergence criterion for velocity is 10^{-6} . For more details on the IC and ILU pre-conditioners refer to [52–56].

The mesh motion solver uses PCG solver with a IC pre-conditioner and its convergence criteria is 10^{-8} . More details on the numerical schemes and algorithms can be found in Bos [33], Kassiotis [44] and OpenFOAM user guide [42].

The pressure–velocity coupling equation is established using the PIMPLE algorithm which combines both PISO [57] and SIMPLE [58] algorithms, enhancing thus the accuracy of the numerical simulations especially when using large time steps in a moving mesh.

3.2. Implicit coupling approach with second order predictor

The exchange of information, mainly pressure and stress, between the fluid domain and the solid structure is done by using a linear point-to-point interpolation [34,35,39] at the fluid structure interface. However, as both fluid and structure solvers use a finite volume method, the data in each field are stored in the cell centers. Therefore, a linear volume-to-point interpolation is performed in each field before the transfer of information from the fluid domain to the solid structure, and vice versa.

The partitioned approach used in the present study results in a communication between three different solvers; fluid flow solver,

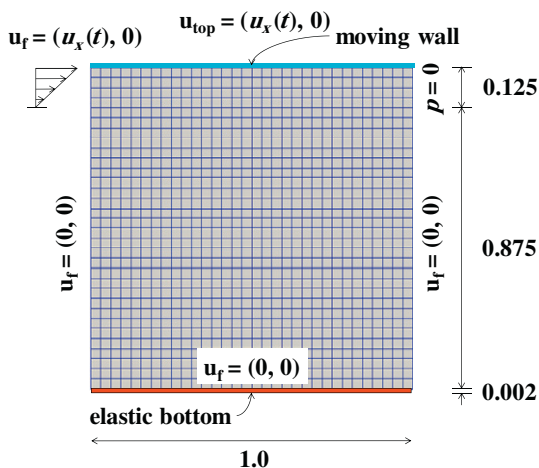


Fig. 2. Geometry and boundary conditions for the lid-driven cavity; dimensions are in meters.

Table 1

Physical properties for the fluid and solid domains for the lid-driven cavity test case.

Solid	ρ_s	(kg m ⁻³)	500
	v_s	(–)	0
	E	(Pa)	250
Fluid	ρ_f	(kg m ⁻³)	1
	v_f	(m ² s ⁻¹)	0.01
Flow	$\bar{u}_{f,inlet}$	(m s ⁻¹)	0–2
	Re	(–)	0–200

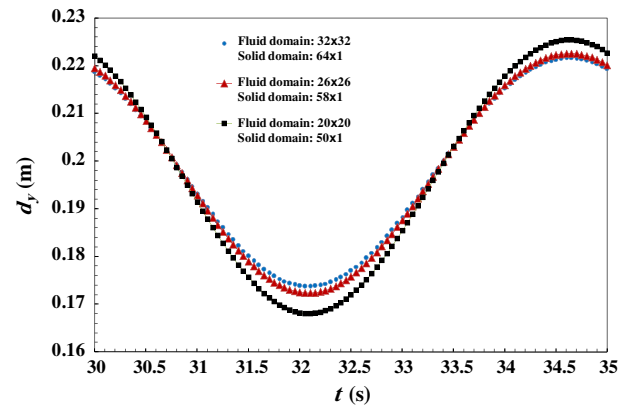


Fig. 3. Time history of the vertical displacement of the flexible bottom midpoint for different mesh densities in both fluid and solid domains.

structural deformation solver and mesh motion solver. As the present study deals with strong coupling interaction between viscous fluid flow and elastic structural material, an iterative implicit fixed-point algorithm with dynamic relaxation [20,29] is used to couple accurately the different solvers and to enforce the equilibrium on the fluid–structure interface. This iterative algorithm is executed at each time step, where, in every outer iteration j , the fluid and structure fields are solved until fulfilling convergence criterion. The flowchart of the numerical procedure developed in the present study is represented in Fig. 1.

Let $\mathbf{d}_{i,j}^r$ the interface displacement at time step ik and for outer iteration j , F the fluid solver, S the solid solver and M the mesh motion solver. For each time step and for $j = 1$, an interface displacement predictor $\tilde{\mathbf{d}}^r$ is used to improve the convergence and performance of the solver:

$$\begin{aligned} \text{Order 0: } \tilde{\mathbf{d}}_{i+1,1}^r &= \mathbf{d}_{i,N}^r \quad \text{for } i = 1 \\ \text{Order 1: } \tilde{\mathbf{d}}_{i+1,1}^r &= \mathbf{d}_{i,N}^r + \delta t \mathbf{u}_{i,N}^r \quad \text{for } i = 2 \\ \text{Order 2: } \tilde{\mathbf{d}}_{i+1,1}^r &= \mathbf{d}_{i,N}^r + \frac{\delta t}{2} (3\mathbf{u}_{i,N}^r - \mathbf{u}_{i-1,N}^r) \quad \text{for } i \geq 3 \end{aligned} \quad (23)$$

where N is the last number of iterations ($j = 1-N$). These equations are initialized at the second step in Fig. 1.

Then the mesh is moved using the predicted interface displacement as boundary condition, and the new internal mesh motion velocity is obtained and then transferred to the fluid flow solver. Next, the fluid flow problem is solved in ALE formulation, using PIMPLE algorithm for pressure–velocity coupling. Then the pressure and viscous stresses are computed and transferred to the fluid–structure interface as boundary conditions for the solid solver. The solid solver is executed to find the predicted displacement $\mathbf{d}_{i+1,j+1}^r = S \circ F(\tilde{\mathbf{d}}_{i+1,j}^r)$. When the stiffness of the solid structure is very small or the ratio of the fluid density to the solid density is large, the impact of the fluid flow on the structure will be very important and thus the predicted interface displacement will not match the result $\tilde{\mathbf{d}}_{i+1,j+1}^r \neq \mathbf{d}_{i+1,j}^r$. Therefore, an iterative correction

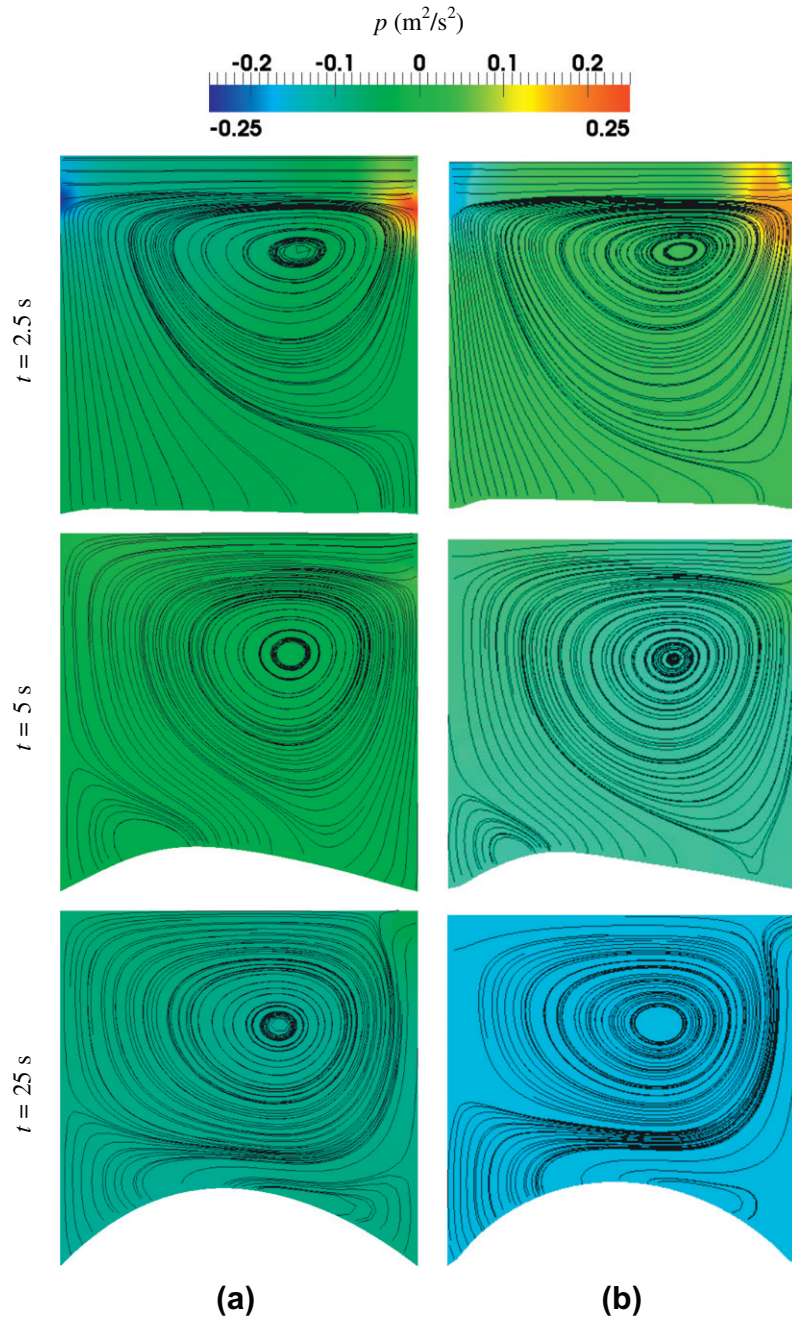


Fig. 4. Snapshots at different time steps of the pressure field and streamlines in the lid-driven cavity: present solution (a) compared to results obtained by Kassiotis et al. [18] (b).

of the interface displacement must be used. This iterative approach can be represented by:

$$\mathbf{d}_{i+1,j+1}^r = \mathbf{d}_{i+1,j}^r + \alpha_{i+1,j+1} \mathbf{r}_{i+1,j+1}^r \quad (24)$$

where $\mathbf{r}_{i+1,j+1}^r = \tilde{\mathbf{d}}_{i+1,j+1}^r - \mathbf{d}_{i+1,j}^r$ is the interface residual and $\alpha_{i+1,j+1}$ is the relaxation parameter.

The iterative procedure requires stopping criteria; therefore, an outer-loop relative error is defined by the length scaled Euclidian norm of the interface displacement residual $\mathbf{r}_{i+1,j+1}^r$ adapted from [18,20,59]:

$$\zeta_{i+1,j+1}^r = \frac{\|\mathbf{r}_{i+1,j+1}^r\|_{\max}}{\sqrt{n_{eq}}} \quad (25)$$

where n_{eq} is the length of the vector $\mathbf{r}_{i+1,j+1}^r$, which is in this case $n_{eq} = 3$. This equation is computed in the step just before the convergence test in Fig. 1. The stopping value for the outer-loop iterations is fixed at $\zeta_{i+1,j+1}^r = 10^{-7}$. Below this value, the outer iterations stop and a new time step begins.

The dynamic relaxation parameter $\alpha_{i+1,j+1}$ is evaluated in every iteration j by using the Aitken Δ^2 method given by Irons and Tuck [29] and revisited recently by Kuttler and Wall [20]. This method uses two previous iterations to determine the current solution. Thus considering $\mathbf{r}_{i+1,j+1}^r = \tilde{\mathbf{d}}_{i+1,j+1}^r - \mathbf{d}_{i+1,j}^r$ and $\mathbf{r}_{i+1,j+2}^r = \tilde{\mathbf{d}}_{i+1,j+2}^r - \mathbf{d}_{i+1,j+1}^r$, the relaxation parameter reads:

$$\alpha_{i+1,j+1} = -\alpha_{i+1,j} \frac{(\mathbf{r}_{i+1,j+1}^r)^T \cdot (\mathbf{r}_{i+1,j+2}^r - \mathbf{r}_{i+1,j+1}^r)}{|\mathbf{r}_{i+1,j+2}^r - \mathbf{r}_{i+1,j+1}^r|^2} \quad (26)$$

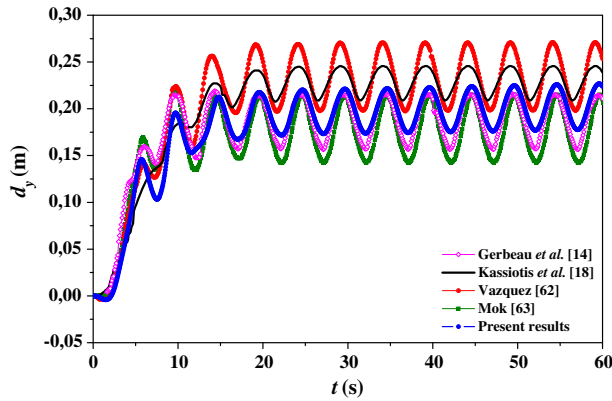


Fig. 5. Time history of the vertical displacement of the flexible bottom midpoint.

Table 2

Numerical approach used in the literature for the lid-driven cavity.

Author	Fluid flow	Structural deformation	Coupling approach
Gerbeau et al. [14]	Stabilized FEM	FEM	Partitioned QN ^a
Kassiotis et al. [18]	FVM ^b	FEM ^c	Partitioned BGS ^d
Vazquez [60]	Stabilized FEM	FEM	Partitioned BGS
Mok [61]	Stabilized FEM	FEM	Partitioned BGS
Present study	FVM	FVM	Partitioned BGS

^a Quasi-Newtonian.

^b Finite volume method.

^c Finite element method.

^d Block Gauss–Seidel.

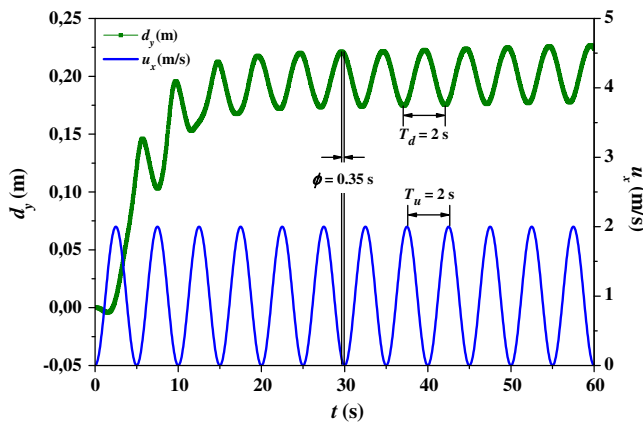


Fig. 6. Time history of the vertical displacement of the flexible bottom midpoint and of the upper wall velocity and of the flow inlet velocity.

As two previous iterations are required, the relaxation parameter for the first under-relaxation cycle $\alpha_{i+1,1}$ cannot be calculated. Moreover, the last relaxation parameter from the previous time step $\alpha_{i,N}$ may be too small to use as first value for the next time step. Therefore, it is suggested [20,29] to use a constrained parameter α_{\max} and hence:

$$\alpha_{i+1,1} = \max(\alpha_{i,N}, \alpha_{\max}) \quad (27)$$

This equation is initialized at the first step in Fig. 1.

The Aitken acceleration method is extensively used in partitioned fluid–structure interaction problems since it is easy to

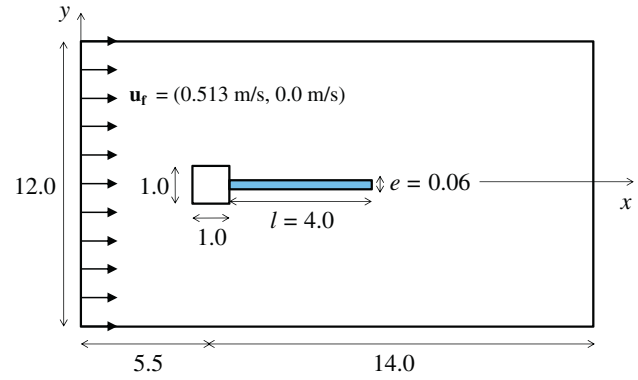


Fig. 7. Computational domain of the elastic cantilever attached to a square bluff body; dimensions in cm.

Table 3

Physical properties for the fluid and solid domains of the benchmark consisting on an elastic cantilever attached to a square bluff body.

Solid	ρ_s	(kg m ⁻³)	100
	ν_s	(–)	0.35
	E	(Pa)	2.5×10^5
Fluid	ρ_f	(kg m ⁻³)	1.18
	ν_f	(m ² s ⁻¹)	1.54×10^{-5}
Flow	$\bar{u}_{f, \text{inlet}}$	(m s ⁻¹)	0.513
	Re	(–)	333

implement and show efficient improvement in result accuracy and simulation time [17,20,27].

4. Numerical validation and examples

In this section, two different benchmarks are used to validate the present results. In the first, the fluid–structure interaction is mainly governed by convective flow motion in a square lid-driven cavity. In the second, the structure deformations are induced by an unsteady vortex shedding mechanism downstream from a bluff body. Finally, a more complex case is studied, and which consists of two elastic flaps in an oscillatory flow. This third case involves not only the influence of the flow on the elastic deformations, but also the influence of both flap oscillations between each other. This third case can also provide a new benchmark for fluid–structure interaction problems.

4.1. Lid-driven cavity with flexible bottom

The present benchmark, shown in Fig. 2, consists on a two dimensional laminar flow in a square cavity with a flexible bottom membrane. This configuration is widely used for the validation of numerical solvers for fluid–structure interaction problems [18]. An oscillatory horizontal velocity $u_x(t)$ is set on the top wall and at the flow inlet at the upper left corner:

$$u_x(t) = 1 - \cos\left(\frac{2\pi}{5}t\right) \quad (28)$$

yielding to velocity oscillations between $u_x = 0$ m/s and $u_x = 2$ m/s.

Both fluid and solid domains are initially at rest. No slip boundary condition and a Neumann zero for the pressure are set on all the other boundaries except for the outlet which is considered to be zero pressure and Neumann zero for velocity.

The bottom of the cavity consists of a flexible membrane which physical properties are given in Table 1. The solid membrane is

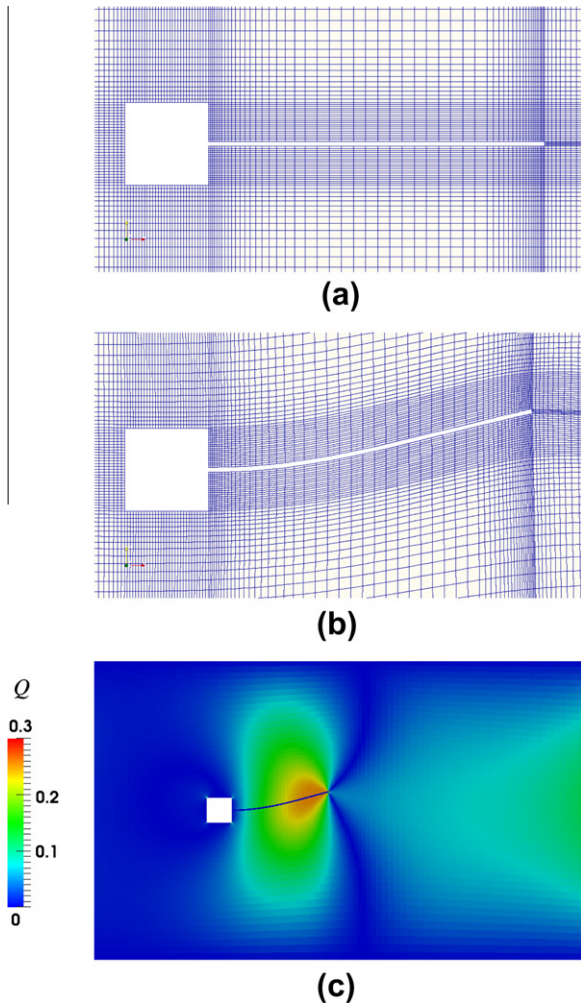


Fig. 8. Mesh of the computational domain at (a) $t = 0$ s and (b) $t = 3.975$ s. The mesh equiangle skew Q for $t = 3.975$ is represented in (c).

discretized by 64×1 cells and the fluid domain is discretized with 32×32 quadrilateral cells, which is sufficient to get accurate results [18,60]. In fact, mesh tests were performed for different mesh densities in both fluid and solid domains. Fig. 3 represents the vertical displacement of the flexible bottom midpoint for three mesh densities. The relative error on the maximum value of d_y reaches 0.4% and 0.1% on the average value for the second mesh density and thus from this grid there is no significant effect of the cell number on the physical results. Other mesh convergence tests have been performed for the next two cases in Sections 4.2 and 4.3, but due to lack of space results are not presented.

The initial Aitken's under relaxation parameter is set to 0.1. The convergence tolerance 10^{-8} for the interface displacement was reached after 6–10 iterations, whereas 15–18 iterating loop were needed when using fixed relaxation parameter equal to 0.1, and thus more computation time is needed. It should be noted that when using weakly coupled scheme, i.e. without outer loop iterations, the solution becomes unstable after few time steps, at $t \approx 2$ s, and it diverges afterwards.

The oscillating boundary conditions, at the flow inlet and on the top wall, produce an unsteady variation of the velocity and pressure field in the cavity which induces an oscillatory deformation of the flexible bottom. Snapshots of the pressure field and streamlines are presented in Fig. 4 for three different time steps and are compared to the results obtained by Kassiotis et al. [18]. As it can be observed from the streamlines, the fluid in the cavity undergoes rotating motion due to the upper moving wall. This convective motion induces thus the deformation of the bottom membrane. This figure shows a good agreement with previous results by Kassiotis et al. [18] where fluid flow was discretized by finite volume method (FVM), and finite element method (FEM) was used for the solid part.

Fig. 5 shows the time history of the bottom midpoint vertical displacement obtained from the present solver and compared to previous results from the open literature [14,18,60,61] using different numerical approaches as presented in Table 2. The present results fall in between those obtained from the literature and are close to those obtained by Gerbeau et al. [14]. Despite the difference in the amplitude of the mean vertical displacement, the period of all the solutions is found almost the same and ranges between 4.9 s and 5.1 s. The oscillations amplitude varies between 7.4 cm for Vazquez [60] and 3.6 cm for Kassiotis et al. [18], while the amplitude for present results is 4.9 cm.

Fig. 6 presents the temporal evolution of the vertical midpoint displacement. The velocity of the top wall and flow inlet u_x , given in Eq. (28), is also reported. In the time interval $0 < t < 17$ s, the flow is in its developing phase after which the membrane displacement reaches its periodical variation from $t \approx 17$ s. The oscillation period of both velocity u_x and displacement d_y is found to be the same ($T_d = T_u = 2$ s) because in such configuration the membrane deformation is directly induced by the velocity field in the cavity which is, in its turn, induced by the boundary velocity $u_x(t)$ in the upper region of the cavity. It is also observed that the maximal deformation amplitude is obtained when the velocity is minimal $u_x(t) = 0$ m/s and the membrane is further pushed down when $u_x(t)$ increases as it lead to increase the forces acting on the membrane. The phase difference between u_x and d_y reaches $\varphi = 0.35$ s, $\varphi/T = 0.175$, which is the duration of the structural deformation response to the velocity variation.

The correlation between $u_x(t)$ and $d_y(t)$ can be evaluated by the mean of Pearson's correlation coefficient defined in Eq. (29):

Table 4

Comparison of current results with those in the open literature for the elastic cantilever attached to square bluff body case.

Author	Fluid flow	Structural deformation	Coupling approach	f (s ⁻¹)	$d_{y,tip}$ (cm)
Kassiotis et al. [18]	FVM	FEM	Partitioned BGS	2.98	1.05
Wood et al. [21]	FVM	FEM	Partitioned BGS	2.94	1.15
Yvin [28]	FVM	FEM	Partitioned BGS	3.16	1.20
Olivier et al. [36]	FVM	FVM	Partitioned BGS	3.17	0.95
Walhorn et al. [63]	Stabilized FEM	FEM	Partitioned BGS	3.14	1.02
Wall [64]	Stabilized FEM	FEM	Partitioned BGS	2.99	1.22
Matthies and Steindorf [65]	FVM	FEM	Partitioned BN ^e	3.13	1.18
Dettmer and Peric [66]	Stabilized FEM	FEM	Partitioned NR ^f	3.03	1.25
Present study	FVM	FVM	Partitioned BGS	3.25	1.02

^e Block-Newton.

^f Newton–Raphson.

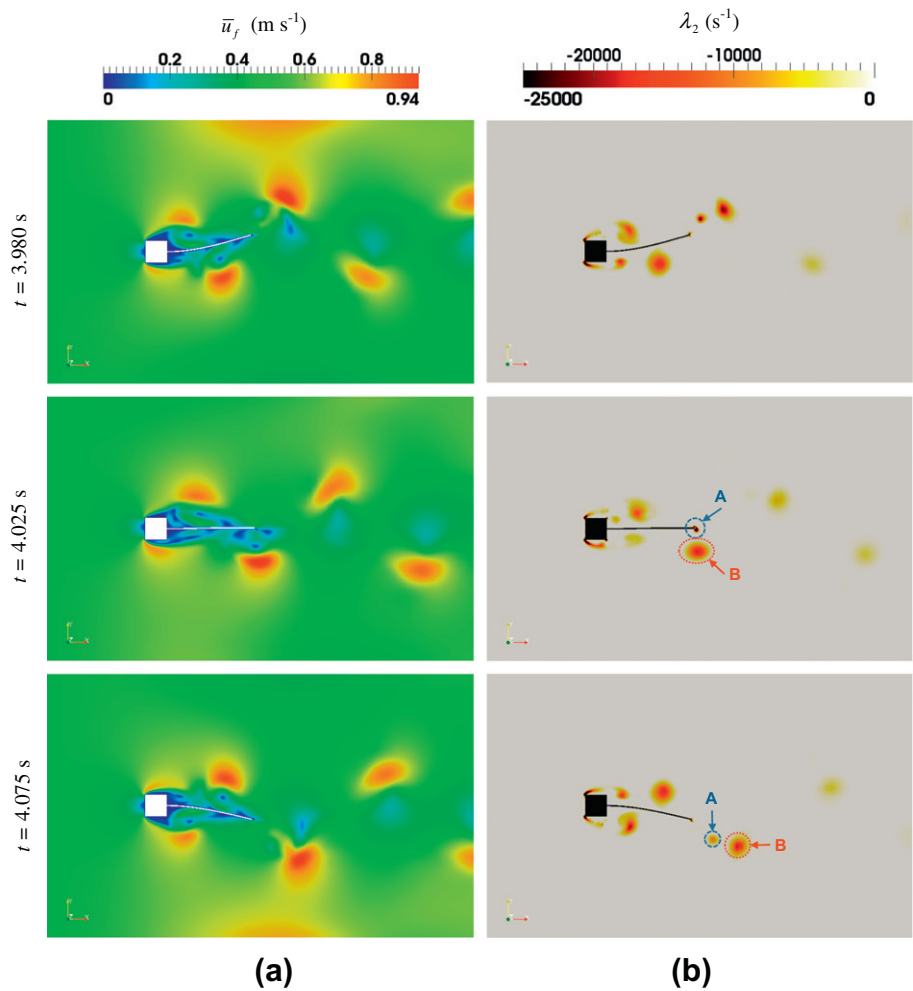


Fig. 9. Snapshots of (a) the mean flow velocity \bar{u}_f and (b) λ_2 criterion for three different time steps.

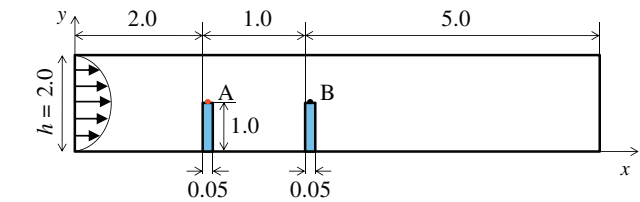


Fig. 10. Sketch of the computational domain for two elastic flaps immersed in a pulsatile flow; dimensions in meters.

$$\Upsilon = \frac{\sum_{i=1}^n [u_x(t) - \bar{u}_x][d_y(t) - \bar{d}_y]}{(n-1)S_{u_x}S_{d_y}} \quad (29)$$

Pearson's correlation coefficient for the two functions u_x and d_y reaches $\Upsilon = -0.855$ and it is evaluated in the periodic region for $17\text{ s} < t < 60\text{ s}$. This negative and relatively high correlation

coefficient value is an evidence of the strong correlation with negative association between the two functions u_x and d_y . Negative association means that positive values of u_x are associated with negative values of d_y .

4.2. Elastic cantilever attached to a square bluff body

While the structural elastic deformation in the previous case is dominated by convective effects, the case shown in Fig. 7 represents a vortex excited elastic flap; a benchmark also widely used for the validation of fluid–structure interaction solvers [18,21,28,36,64–67].

This benchmark consists on an elastic cantilever attached to a fixed square bluff body immersed in an incompressible flow which is initially at rest. The top and bottom boundaries are considered

Table 5
Physical properties for the fluid and solid domains of the benchmark consisting on two elastic flaps immersed in a pulsatile flow.

			TFP1	TFP2
Solid	ρ_s	(kg m ⁻³)	1000	1000
	ν_s	(–)	0.3	0.3
	E	(Pa)	1×10^6	1×10^5
Fluid	ρ_f	(kg m ⁻³)	100	100
	ν_f	(m ² s ⁻¹)	0.001	0.001
Flow	$\bar{u}_{f,max,inlet}$	(m s ⁻¹)	0.25–0.50	0.25–0.50
	Re	(–)	500–1000	500–1000

symmetry planes. The flow is uniformly distributed at the inlet (on the left hand side in Fig. 7) with an imposed streamwise mean velocity $\bar{u}_{inlet} = 0.513$ m/s. The outlet is considered to be zero pressure and Neumann zero for velocity. This velocity corresponds to a Reynolds number $Re = u_{x,inlet}r/\nu_f = 333$, based on the bluff body dimension $r = 1$ cm, which is higher than the critical Reynolds number beyond which the flow separation from the square corners produces a transient Von Karman vortex street [18,28]. This transient behavior of the flow induces thus a periodic variation of the pressure and viscous stress fields in the near wake of the bluff body which in turns induces the oscillations of the elastic appendix. The physical properties of the fluid and solid domains, represented in Table 3, are chosen so that the vortex shedding frequency is close to the first Eigen-frequency of the elastic appendix which is 3.03 s $^{-1}$ [18].

The fluid domain contains 15726 quadrilateral cells with mesh refined on all solid boundaries. The solid structure domain contains 2000 quadrilateral cells. The initial mesh of the fluid domain is represented in Fig. 8a showing the grid refined at the wall of the square bluff body and near the fluid–structure interface. Fig. 8b shows the deformed mesh for the time step $t = 3.975$ s where good mesh quality is always maintained. This quality is represented by the mean of the equi-angle skew Q in Fig. 8c where it is shown that its maximal value does not exceed 0.3 emphasizing good mesh quality. The solution in the new generated non-orthogonal cells is corrected in the PIMPLE algorithm. To reach the tolerance on the interface displacement (Eq. (25)), a maximum number of three iterations was required. The initial value of the Aitken's under relaxation parameter is fixed at 0.3 which rapidly increases to 0.9.

The oscillations frequency and the maximal displacement of the cantilever tip are represented in Table 4. A good agreement is found with previous results from the open literature. The mean frequency of the cantilever oscillation 3.25 s $^{-1}$ is very close to the theoretical Eigen-frequency of the elastic appendix which is 3.03 s $^{-1}$ as its motion is dominated by the first beam Eigen-frequency. The maximal tip motion obtained here $d_y = 1.02$ cm is close to

those obtained from the open literature by using different solvers, and which ranges between 0.95 cm and 1.25 cm.

The velocity snapshots represented in Fig. 9a for three different time steps show an unsteady behavior of the flow which leads, as consequence, to unsteady oscillations of the elastic cantilever. These oscillations induce in their turn velocity gradients in the flow, near the cantilever tip, which results in the generation of new vortices. These vortices can be highlighted by using the λ_2 criterion introduced by Jeong and Hussain [62].

Fig. 9b represents the snapshots of $\lambda_2 < 0$ where the vortex core can be observed downstream from the bluff body. It can be observed that the Von Karman vortex street generated by the square bluff body is dispersed towards the upper and lower regions due to the flapping of the elastic cantilever. Moreover, the flap oscillations generates velocity gradients at its tip, thus causing the development of transient vortices, denoted A and B, advecting downstream from the flap.

4.3. Two elastic flaps immersed in pulsatile flow

In this section, two elastic flaps immersed in a pulsatile flow are considered as shown in Fig. 10. Both elastic flaps have the same physical properties as given in Table 5. Similar properties were also used by Olivier and Dumas [16] and Olivier et al. [36] for the case of one vertical flap in a uniform channel flow. Two different cases are studied, TFP1 and TFP2, which differs by the Young modulus value: in the case TFP2 the Young modulus is 10 times smaller than in TFP1 (see Table 5).

The aim of this study is to present a more complex case where the elastic flaps deformation follow a chaotic behavior independent of the main flow velocity oscillations at the channel inlet.

No slip boundary conditions are set on the two flaps fluid/structure interfaces and on the channel top and bottom walls. The outlet is set at zero pressure and zero Neumann for velocity, and a pulsatile parabolic velocity profile is set at the flow inlet following a smooth increase from $t = 0$ s to $t = 1$ s:

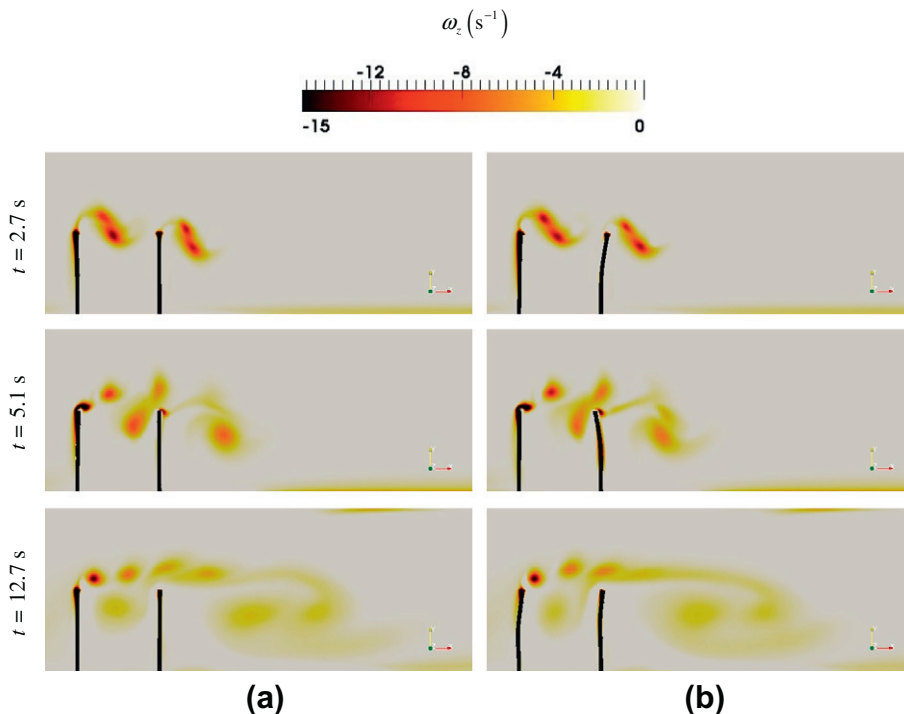


Fig. 11. Snapshots of the vorticity ω_z for both cases (a) TFP1 and (b) TFP2 for three different time steps.

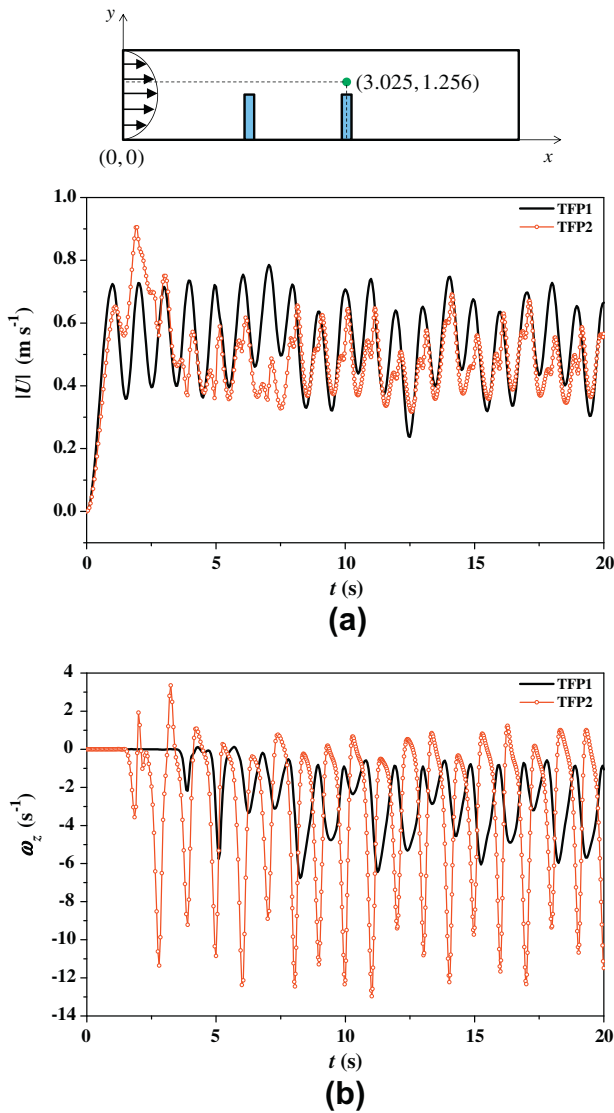


Fig. 12. Time history of (a) the velocity magnitude and (b) the vorticity field in the point (3.025, 1.256).

$$u_{f,inlet} = \frac{\bar{u}_{f,inlet}}{2} [1 - \cos(\pi t)] \quad \text{for } t < 1 \text{ s} \quad (30)$$

$$u_{f,inlet} = \frac{\bar{u}_{f,inlet}}{4} [3 + \cos(2\pi t)] \quad \text{for } t \geq 1 \text{ s} \quad (31)$$

where $\bar{u}_{f,inlet} = u_{\max} y(h - y)$ for $0 < y < h$ and with $u_{\max} = 0.5$ m/s. Thus, the resulting Reynolds number $Re = \bar{u}_{f,max,inlet} h / \nu_f$, where $\bar{u}_{f,max,inlet} = \bar{u}_{f,inlet}(x = 0, y = h/2, t)$ is the inlet velocity at the channel center, for $t \geq 1$ s oscillates between 500 and 1000 with a period $T_{Re} = 1$ s.

It should be noted here that the smooth increase in the flow velocity is important for better numerical stability at the start of the simulations and to avoid having a brutal shock on the structure. This method is commonly used in other fluid–structure interaction problems [67].

The fluid domain mesh consists of 9480 quadrilateral cells refined near the wall and fluid–structure interfaces. Each solid structure mesh is composed of 1000 quadrilateral cells. The initial value of the Aitken's relaxation parameter is set to 0.1 and a maximal number of 12 iterations were needed to reach the convergence criterion for the fluid–structure interface displacement.

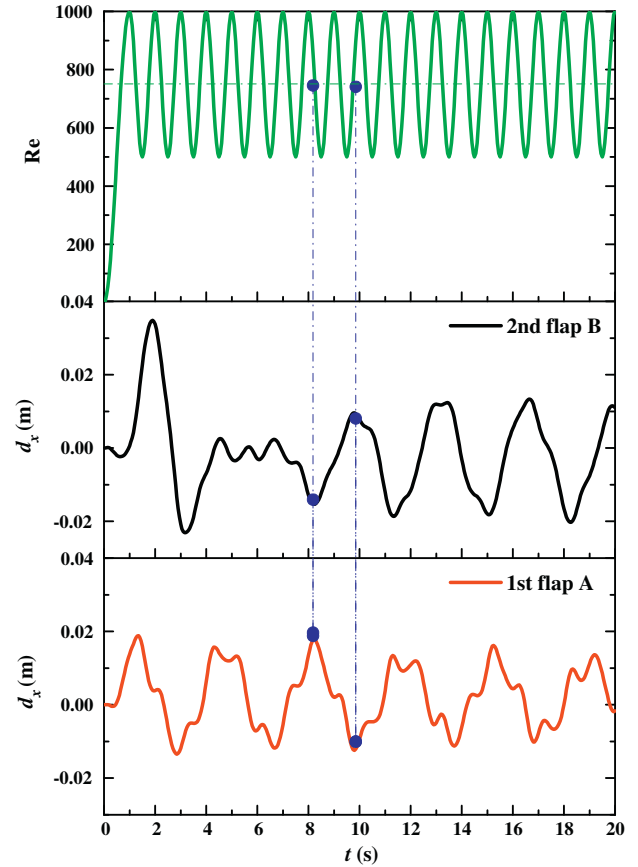


Fig. 13. Temporal variation of the Reynolds number and of the horizontal displacement of the tip of both flaps A and B for the case TFP1.

Fig. 11 shows snapshots of the vorticity field ω_z for three different time steps and for both cases TFP1 and TFP2. When the flow encounters the flaps, a shear layer is formed at their tips, due to velocity gradients between the accelerating fluid in the flow core and the low momentum fluid in the wake region downstream the flaps. This shear layer is further deformed and detached due to shear instability of Kelvin–Helmholtz type. Owing to the pulsatile nature of the inlet flow velocity, a periodic sequence of vortices is then formed at which flap tip as shown on Fig. 11 from high values of negative ω_z (negative values means that the vortices are rotating in the clockwise direction). It can be noticed that larger structural deformation is observed in TFP2 as the structure stiffness is lower than in TFP1, and thus it has weaker resistance to the fluid flow.

Comparing Fig. 11a and b for time steps larger than 2.7 s, it can be observed that the flow topology differs in both case (TFP1 and TFP2) due to some difference in the shedding of perturbations induced by the flaps oscillations on the development and convection of the vortices. This difference can be quantitatively observed from the time history analysis of the velocity magnitude and normal vorticity shown in Fig. 12a and b respectively for a given point located above the second flap at (3.025, 1.556). The Pearson's correlation coefficient between the inlet velocity and the velocity near the flap is computed using the same approach as in Eq. (29) after replacing d_y by $u_{f,inlet}$ and u_x by the velocity magnitude in the given point. Its value which reaches $Y_{TFP1} = 0.926$, for the case TFP1, indicates very strong correlation while for TFP2 the correlation coefficient is much smaller $Y_{TFP2} = 0.658$. The weaker correlation for TFP2 is caused by larger influence of the flap oscillations on the flow field near the second flap which add perturbation velocities

to the main flow which is essentially related to the pulsatile inlet flow. This can be also observed from the variation of the velocity magnitude in Fig. 12a, where it represents a quasi-periodic variation for TFP1 with a time period $T \approx 1$ s almost the same as that at the inlet flow velocity. Meanwhile, a quasi-chaotic behavior for TFP2 is observed with no characteristic frequency.

The time history of the normal vorticity in Fig. 12b also shows an important difference between both cases TFP1 and TFP2. Larger vorticity values are obtained in the vicinity of TFP2 as the higher oscillations induces largest perturbation to the flow and thus increase the velocity gradients in the shear layer, which are the principal cause for the development of the vortex structures as explained above.

The time history of the horizontal displacement of the tip of the two flaps is represented in Figs. 13 and 14 respectively for TFP1 and TFP2 cases. Largest oscillation amplitudes with higher frequencies are found in TFP2 relative to TFP1 for both flaps. The Pearson's correlation coefficient between the Reynolds number and the displacement is almost $Y \approx 0$ for both flaps in both cases. This means that there is no correlation between the pulsatile flow and the flaps oscillations. These oscillations are indeed caused by the local vortex shedding near the flaps, which is caused by the vortices in the flow.

Meanwhile, by observing the blue dotted lines in Fig. 13, a negative correlation is obtained between the flaps displacement in TFP1 $\gamma_{d_{A-B,TFP1}} = -0.628$ (calculated for $t > 8$ s). Negative correlation is found as the maximal displacement of the flap tip A are associated with minimal displacement of the flap tip B because the oscillations are in opposite phase. Contrarily, in the case of TFP2, the correlation coefficient is $\gamma_{d_{A-B,TFP2}} = 0.667$ as the flaps displacements are in-phase. This result can be explained by the fact that

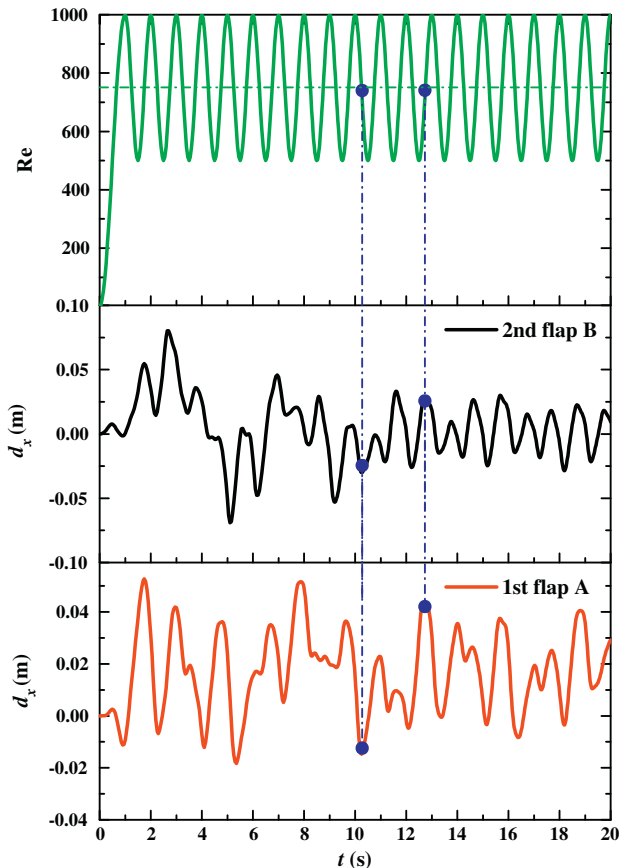


Fig. 14. Temporal variation of the Reynolds number and of the horizontal displacement of the tip of both flaps A and B for the case TFP2.

in case TFP2, the flaps are more flexible than in the case TFP1, and thus when the first flap moves toward the second one, it will entrain with it a mass of fluid which moves the second flap in the same direction.

5. Conclusions

A partitioned solver is developed in the present study taking into account strong coupling fluid–structure interaction problems by using block Gauss–Seidel implicit scheme with adaptive Aitken's relaxation. The use of such approach is fundamental in the case of partitioned methods where different solvers for the fluid flow and the structural deformation are communicating at the fluid–structure interface.

Finite volume method is used to discretize both fluid flow and structural displacement. The Navier–Stokes equations are solved in an Arbitrary Lagrangian–Eulerian formulation as the internal mesh in the flow region is deforming with the flexible boundaries. As the present study deals with elastic flaps interacting with viscous flows, the Lagrangian formulation using the St. Venant–Kirchhoff constitutive law was discretized in an iterative segregated approach. The communication between the flow and the structural solvers is achieved on the fluid–structure interface. The mesh motion solver, which uses the Laplace smoothing equation with variable mesh diffusivity, takes the displacement at the fluid–structure interface as a boundary condition and solves the internal mesh motion in the fluid domain. This solver called vorflexFoam was developed by using the open source C++ library OpenFOAM.

At first, the well-known lid-driven cavity with flexible bottom benchmark was used to validate the solution obtained by using vorflexFoam. A good agreement between the present results and those obtained from the open literature is observed despite the difference between the discretization methods and the solution algorithms. The analysis of the correlation between the pulsatile boundary velocity and the flexible membrane deformation underlines the fact that the structural deformations are mainly caused by the incompressibility effects and the convective flow in the cavity.

Another benchmark is also used to validate the present solver, where the elastic flap deformation is excited by a Von Karman vortex street shedding from a square bluff body. The results also show a good agreement with those obtained from the open literature, and the flow analysis shows that the interaction is done in both directions: the unsteady vortices induce a periodic flap deformation, which in its turn interact with the neighbor fluid generating new vortices at the flap tip, and dispersing the Von Karman vortex street away from its classical path.

At the end, a more complex case is represented consisting of two flaps inserted in a pulsatile flow. Two cases are considered differing by the Young modulus. These flaps are found to oscillate in opposite-phase for the higher Young modulus, and in-phase for the lower one. It is shown that lower solid stiffness lead also to higher amplitude and frequency in the flaps oscillations inducing larger perturbation to the flow and thus breaking the flow regularity when observing the time history of the velocity in a given point of the flow. In fact, these oscillations interact with the vortices ejected from the flaps tips, due to instability of Kelvin–Helmholtz type, and increase the velocity gradients and thus the instability in the shear layer. This complex fluid–structure interaction induces, for optimal material properties, a chaotic flow behavior near the flaps.

Future study will consider the use of elastic flap oscillations for the enhancement of the heat and mass transfer in multifunctional heat exchangers/reactors as these oscillations tend to break the regularity of the flow and to generate a chaotic advection.

Acknowledgements

This work is financially supported by the PIE-VORFLEX, CNRS, France. Fruitful discussion with Dr. Sebastien Vintrou and Dr. Sebastien Menanteau from EMDouai-El are gratefully acknowledged. The authors would like also to acknowledge Prof. Guy Dumas and Mr. Mathieu Olivier from Laval University, Quebec, Canada for enlightening discussions and for providing details on their numerical simulations.

References

- [1] Newman DJ, Karnidakis GE. A direct numerical simulation study of flow past a freely vibrating cable. *J Fluid Mech* 1997;344:95–136.
- [2] Evangelinos C, Karnidakis GE. Dynamics and flow structures in the turbulent wake of rigid and flexible cylinders subject to vortex-induced vibrations. *J Fluid Mech* 1999;400:91–124.
- [3] Parolini N, Quarteroni A. Mathematical models and numerical simulations for the America's Cup. *Comput Methods Appl Mech Eng* 2005;194:1001–26.
- [4] Lambert RA, Rangel RH. The role of elastic flap deformation on fluid mixing in a microchannel. *Phys Fluids* 2010;22(5):052003.
- [5] Habchi C, Lemenand T, Della-Valle D, Peerhossaini H. Turbulence behavior of artificially generated vorticity. *J Turbul* 2010;11(36):1–18.
- [6] Razzaq M, Damanik H, Hron J, Ouazzi A, Turek S. FEM multigrid techniques for fluid-structure interaction with application to hemodynamics. *Appl Numer Math* 2012;62(9):1156–70.
- [7] Crossetto P, Reymond P, Delpar S, Kontaxakis D, Stergiopoulos N, Quarteroni A. Fluid-structure interaction simulation of aortic blood flow. *Comput Fluids* 2011;43(1):46–57.
- [8] Greenshields CJ, Weller HG. A unified formulation for continuum mechanics applied to fluid-structure interaction in flexible tubes. *Int J Numer Methods Eng* 2005;64(12):1575–93.
- [9] Walhorn E, Kolke A, Hubner B, Dinkler D. Fluid-structure coupling within a monolithic model involving free surface flows. *Comput Struct* 2005;83(25–26):2100–11.
- [10] Heil M, Hazel A, Boyle J. Solvers for large-displacement fluid-structure interaction problems: segregated versus monolithic approaches. *Comput Mech* 2008;43:91–101.
- [11] Badia S, Quaini Q, Quarteroni A. Modular vs. non-modular preconditioners for fluid-structure systems with large added-mass effect. *Comput Methods Appl Mech Eng* 2008;197:4216–32.
- [12] Cirak F, Deiterding R, Mauch SP. Large-scale fluid-structure interaction simulation of viscoplastic and fracturing thin-shells subjected to shocks and detonations. *Comput Struct* 2007;85(11–14):1049–65.
- [13] Karac A, Blackman B, Cooper V, Kinloch A, Sanchez SR, Teo W, et al. Modelling the fracture behaviour of adhesively-bonded joints as a function of test rate. *Eng Fract Mech* 2011;78(6):973–89.
- [14] Gerbeau J-F, Vidrascu M, Frey P. Fluid-structure interaction in blood flows on geometries based on medical imaging. *Comput Struct* 2005;83(2–3):155–65.
- [15] Wall WA, Genkinger S, Ramm E. A strong coupling partitioned approach for fluid-structure interaction with free surfaces. *Comput Fluids* 2007;36(1):169–83.
- [16] Olivier M, Dumas G. Non-linear aeroelasticity using an implicit partitioned finite volume solver. In: Proceedings of the 17th annual conference of the CFD society of Canada, Ottawa, Canada; 2009.
- [17] Degroote J, Haelterman R, Annerel S, Bruggeman P, Vierendeels J. Performance of partitioned procedures in fluid-structure interaction. *Comput Struct* 2010;88(7–8):446–57.
- [18] Kassiotis C, Ibrahimbegovic A, Niekamp R, Matthies H. Nonlinear fluid-structure interaction problem. Part I: implicit partitioned algorithm, nonlinear stability proof and validation examples. *Comput Mech* 2011;47:305–23.
- [19] Tallec PL, Mouro J. Fluid-structure interaction with large structural displacements. *Comput Methods Appl Mech Eng* 2001;190(24–25):3039–67.
- [20] Kuttler U, Wall W. Fixed-point fluid-structure interaction solvers with dynamic relaxation. *Comput Mech* 2008;43:61–72.
- [21] Wood C, Gil A, Hassan O, Bonet J. Partitioned block-Gauss-Seidel coupling for dynamic fluid-structure interaction. *Comput Struct* 2010;88(23–24):1367–82.
- [22] Michler C, van Brummelen EH, de Borst R. An interface Newton Krylov solver for fluid-structure interaction. *Int J Numer Methods Fluids* 2005;47(10–11):1189–95.
- [23] Fernández MA, Moubachir M. An exact Block-Newton algorithm for the solution of implicit time discretized coupled systems involved in fluid-structure interaction problems. In: Bathe KJ, editor. Computational fluid and solid mechanics 2003. Oxford: Elsevier Science Ltd.; 2003. p. 1337–41.
- [24] Fernández MA, Moubachir M. A Newton method using exact Jacobians for solving fluid-structure coupling. *Comput Struct* 2005;83:127–42.
- [25] Degroote J, Vierendeels J. Multi-solver algorithms for the partitioned simulation of fluid-structure interaction. *Comput Methods Appl Mech Eng* 2011;200(25–28):2195–210.
- [26] Causin P, Gerbeau JF, Nobile F. Added-mass effect in the design of partitioned algorithms for fluid-structure problems. *Comput Methods Appl Mech Eng* 2005;194:4506–27.
- [27] Gallinger T, Bletzinger K. Comparison of algorithms for strongly coupled partitioned fluid-structure interaction – efficiency versus simplicity. In: Pereira J, Sequeira A, Pereira JM, editors. Proceedings of the V European conference on computational fluid dynamics ECCOMAS CFD, Lisbon, Portugal; 2010. p. 1–20.
- [28] Yvin C. Partitioned fluid-structure interaction with open-source tools. 12ème Journées de l'Hydrodynamique, Nantes, France; 2010.
- [29] Irons BM, Tuck RC. A version of the Aitken accelerator for computer iteration. *Int J Numer Methods Eng* 1969;1(3):275–7.
- [30] Donea J, Giuliani S, Halleux JP. An arbitrary Lagrangian-Eulerian finite element method for transient dynamic fluid-structure interactions. *Comput Methods Appl Mech Eng* 1982;33:689–723.
- [31] Souli M, Ouahsine A, Lewin L. ALE formulation for fluid-structure interaction problems. *Comput Methods Appl Mech Eng* 2000;190:659–75.
- [32] Donea J, Huerta A, Ponthot J-P, Rodriguez-Ferran A. Arbitrary Lagrangian-Eulerian methods. In: Encyclopedia of computational mechanics. John Wiley & Sons, Ltd.; 2004. p. 413–33 [chapter 14].
- [33] Bos F. Numerical simulations of flapping foil and wing aerodynamics – mesh deformation using radial basis functions. Ph.D. thesis, the Technical University of Delft, Netherlands; 2010.
- [34] Jasak H, Weller HG. Application of the finite volume method and unstructured meshes to linear elasticity. *Int J Numer Methods Eng* 2000;48(2):267–87.
- [35] Tukovic Z, Jasak H. Updated Lagrangian finite volume solver for large deformation dynamic response of elastic body. *Trans FAMENA* 2007;31(1):1–16.
- [36] Olivier M, Dumas G, Morissette J. A fluid-structure interaction solver for nano-air-vehicle flapping wings. In: Proceedings of the 19th AIAA computational fluid dynamics conference, San Antonio, USA; 2009. p. 1–15.
- [37] Bathe K, Hahn W. On transient analysis of fluid-structure systems. *Comput Struct* 1979;10(1–2):383–91.
- [38] Sathe S, Benney R, Charles R, Doucette E, Miletti J, Senga M, et al. Fluid-structure interaction modeling of complex parachute designs with the space-time finite element techniques. *Comput Fluids* 2007;36(1):127–35.
- [39] Jasak H, Tukovic Z. Automatic mesh motion for the unstructured finite volume method. *Trans FAMENA* 2007;30(2):1–18.
- [40] Bos F. Moving and deforming meshes for flapping flight at low reynolds number. In: 3rd OpenFOAM workshop, Milan, Italy; 2008.
- [41] Jasak H, Tukovic Z. Dynamic mesh handling in openfoam applied to fluid-structure interaction simulations. In: Pereira J, Sequeira A, Pereira JM, editors. Proceedings of the V European conference on computational fluid dynamics ECCOMAS CFD, Lisbon, Portugal; 2010. p. 1–19.
- [42] OpenFOAM. The open source CFD toolbox – user guide version 1.7.1; 2010. p. 1–204.
- [43] Weller HG, Tabor G, Jasak H, Fureby C. A tensorial approach to computational continuum mechanics using object-oriented techniques. *Comput Phys* 1998;12:620–31.
- [44] Kassiotis C. Nonlinear fluid-structure interaction: a partitioned approach and its application through component technology. Ph.D. thesis, University Paris Est, France; 2009.
- [45] Jasak H, Jemcov A, Tukovic Z. Openfoam: a c++ library for complex physics simulations. International workshop on coupled methods in numerical dynamics, IUC, Dubrovnik, Croatia; 2007. p. 1–20.
- [46] Kassiotis C, Ibrahimbegovic A, Matthies H. Partitioned solution to fluid-structure interaction problem in application to free-surface flows. *Eur J Mech – B/Fluids* 2010;29(6):510–21.
- [47] Lohner R, Yang C. Improved ale mesh velocities for moving bodies. *Commun Numer Methods Eng* 1996;12(10):599–608.
- [48] Dwight RP. Robust mesh deformation using the linear elasticity equations. In: Deconinck H, Dick E, editors. Computational fluid dynamics 2006. Berlin, Heidelberg: Springer; 2009. p. 401–6.
- [49] Johnson A, Tezduyar T. Mesh update strategies in parallel finite element computations of flow problems with moving boundaries and interfaces. *Comput Methods Appl Mech Eng* 1994;119(1–2):73–94.
- [50] Krause E. Computational fluid dynamics: its present status and future direction. *Comput Fluid* 1985;13(3):239–69.
- [51] Jakobsson S, Amoignon O. Mesh deformation using radial basis functions for gradient-based aerodynamic shape optimization. *Comput Fluids* 2007;36(6):1119–36.
- [52] Ferziger J, Peric M. Computational methods for fluid dynamics. 3rd ed. Berlin: Springer-Verlag; 2002. p. 423.
- [53] Behie A, Collins D, Forsyth Jr P. Incomplete factorization methods for three-dimensional non-symmetric problems. *Comput Methods Appl Mech Eng* 1984;42(3):287–99.
- [54] Sundholm D. A block preconditioned conjugate gradient method for solving high-order finite element matrix equations. *Comput Phys Commun* 1988;49(3):409–15.
- [55] Doi S. On parallelism and convergence of incomplete LU factorizations. *Appl Numer Math* 1991;7(5):417–36.
- [56] Lin CJ, Saigal R. An incomplete Cholesky factorization for dense symmetric positive definite matrices. *BIT Numer Math* 2000;40(3):536–58.
- [57] Issa RI. Solution of the implicitly discretised fluid flow equations by operator-splitting. *J Comput Phys* 1986;62(1):40–65.

- [58] Patankar S, Spalding D. A calculation procedure for heat, mass and momentum transfer in three-dimensional parabolic flows. *Int J Heat Mass Transfer* 1972;15(10):1787–806.
- [59] Deparis S. Numerical analysis of axisymmetric flows and methods for fluid structure interaction arising in blood flow simulation. Ph.D. thesis, EPFL, Lausanne; 2004.
- [60] Vazquez J-G-V. Nonlinear analysis of orthotropic membrane and shell structures including fluid-structure interaction. Ph.D. thesis, Escola Tecnica Superior d'Enginyers de Camins, Universitat Politecnica de Catalunya, Barcelone, Espagne, 2007.
- [61] Mok DP. Partitionierte losungsansatze in der strukturdynamik und der fluid-struktur-interaktion. Ph.D. thesis, Universitat Stuttgart, Holzgartenstr. 16, 70174 Stuttgart; 2001.
- [62] Jeong FHJ, Hussain F. On the identification of a vortex. *J Fluid Mech* 1995;285:69–84.
- [63] Walhorn E, Hubner B, Dinkler D. Space-time finite elements for fluid-structure interaction. *PAMM* 2002;1(1):81–2.
- [64] Wall W-A. Fluid-struktur interaktion mit stabilisierten finiten elementen. Ph.D. thesis, Institut fur Baustatik und Baudynamik, Universitat Stuttgart, Germany; 1999.
- [65] Matthies HG, Steindorf J. Partitioned strong coupling algorithms for fluid-structure interaction. *Comput Struct* 2003;81(8–11):805–12.
- [66] Dettmer W, Peric D. A computational framework for fluid-structure interaction: finite element formulation and applications. *Comput Methods Appl Mech Eng* 2006;195(41–43):5754–79.
- [67] Razzaq M, Hron J, Turek S. Numerical simulation of laminar incompressible fluid-structure interaction for elastic material with point constraints. In: Rannacher R, Sequeira A, editors. *Advances in mathematical fluid mechanics*. Berlin, Heidelberg: Springer; 2010. p. 451–72.